Supporting Information

Restriction of Intramolecular Rotation for Empowering Metal Nanoclusters

Junsheng Xin,[#a,b] Jing Xu,[#a] Chen Zhu,[a] Yupeng Tian,[a] Qiong Zhang,*[a] Xi Kang,*[a,b] Manzhou Zhu*[a,b]

[a]Department of Chemistry and Centre for Atomic Engineering of Advanced Materials, Key Laboratory of Structure and Functional Regulation of Hybrid Materials of Ministry of Education, Anhui University, Hefei, Anhui 230601, China.
[b]Institutes of Physical Science and Information Technology and Anhui Province Key Laboratory of Chemistry for Inorganic/Organic Hybrid Functionalized Materials, Anhui University, Hefei, Anhui 230601, China.

#Junsheng Xin and Jing Xu contributed equally to this work.

*E-mails of corresponding authors: zmz@ahu.edu.cn (M.Z.); kangxi_chem@ahu.edu.cn (X.K.); zhangqiong.314@163.com (Q.Z.)

Notes: The authors declare no competing financial interest.

This Supporting Information includes:
Methods
Figures S1-S21
Tables S1-S4

1. Methods

1.1 Materials.

All following chemicals, including silver nitrate ($AgNO_3$, 99.9%, metal basis), tetrachloroauric(III) acid ($HAuCl_4 \bullet 3H_2O$, ≥99.99%, metals basis), 2,5-dimethylbenzenethiol ($HSPhMe_2$, ≥99.99%), 2,6-dichlorobenzenethiol ($HSPhCl_2$, ≥99.99%), bis (diphenylphosphino)methane ($Ph_2P\text{-}C_2H_5\text{-}PPh_2$, DPPM, 98%), sodium borohydride ($NaBH_4$, 99%), methylene chloride (CH_2Cl_2, HPLC grade), methanol (CH_3OH, HPLC grade), *n*-hexane (Hex, HPLC grade) were purchased from Sigma-Aldrich and used without further purification.

1.2 Synthesis of $Au_4Ag_{13}(DPPM)_3(SPhMe_2)_9$.

The preparation of $Au_4Ag_{13}(DPPM)_3(SPhMe_2)_9$ was based on the reported method.

1.3 Synthesis of $Au_4Ag_{13}(DPPM)_3(SPhCl_2)_9$.

The $Au_4Ag_{13}(DPPM)_3(SPhCl_2)_9$ nanocluster was prepared using the same synthetic procedure as $Au_4Ag_{13}(DPPM)_3(SPhMe_2)_9$, while the thiol ligand source was altered to $HSPhCl_2$.

1.4 Crystallization of $Au_4Ag_{13}(DPPM)_3(SPhMe_2)_9$ and $Au_4Ag_{13}(DPPM)_3(SPhCl_2)_9$ nanoclusters.

The crystallization of the $Au_4Ag_{13}(DPPM)_3(SPhMe_2)_9$ nanocluster was performed based on the reported method. For the $Au_4Ag_{13}(DPPM)_3(SPhCl_2)_9$ nanocluster, single crystals of these nanoclusters were cultivated at room temperature by liquid diffusing the *n*-hexane into the CH_2Cl_2 solution of them. After 14 days, black crystals were collected, and the structures of these nanoclusters were determined.

1.5 X-ray crystallography.

The data collection for single-crystal X-ray diffraction (SC-XRD) of all nanocluster crystal samples was carried out on Stoe Stadivari diffractometer under nitrogen flow, using graphite-monochromatized Cu Kα radiation (λ = 1.54186 Å). Data reductions and absorption corrections were performed using the SAINT and SADABS programs, respectively. The structure was solved by direct methods and refined with full-matrix least squares on F^2 using the SHELXTL software package. All non-hydrogen atoms were refined anisotropically, and all the hydrogen atoms were set in geometrically calculated positions and refined isotropically using a riding model. All crystal structures were treated with PLATON SQUEEZE, and the diffuse electron densities from these residual solvent molecules were removed. The CCDC number of the $Au_4Ag_{13}(DPPM)_3(SPhCl_2)_9$ nanocluster is 2223274.

1.6 Two-photon excited fluorescence (2PEF) spectroscopy and two-photon absorption (2PA) cross-section.

The 2PEF spectra were obtained by the 2PEF method with a femtosecond laser pulse as the light source. All the samples were contained in 1cm-optical length quartz liquid cell. Spectrometer: Ocean Optics QE65 Pro (300-2500 nm). Laser: Coherent Astrella+TOPAS Prime (1100-2700) nm, 1 kHz, 120 fs. The reference sample was Rhodamine 6G (1.0×10^{-3} M). The concentration of the sample was 1.0×10^{-2} and 1.0×10^{-3} M. 2PA cross section was calculated by using the following equation:

$$\delta_{2s=}\frac{c_R \times n_R \times f_s \times Q_R}{c_s \times n_S \times f_R \times Q_S} \times \delta_{2R}$$

Here, R stands for reference, S stands for samples, δ_{2s} is the two-photon absorption cross section, Φ is quantum yield, c is the concentration, n is refractive index, and F is two-photon fluorescence integral area. The absolute value of the two-photon absorption cross section of the reference sample is derived from the literature.[1]

1.7 Three-photon excited fluorescence (3PEF) spectroscopy.

All the samples were contained in 1-cm-thick quartz cuvette and the Rhodamin 6G was used as the standard sample for the intensity comparison. Spectrometer: Ocean Optics QE65 Pro (300-2500 nm). Laser: Coherent Astrella+TOPAS Prime (1100-2700, for <1600nm is signal laser, for >1600 nm is idler laser), 1 kHz, 120 fs. The reference sample was Rhodamine 6G. The concentration of the sample was 1.0×10^{-4} mol/L.

Theory:

$$\sigma_{3s=}\frac{c_R \times n_s \times f_s \times Q_R}{c_s \times n_R \times f_R \times Q_S} \times \sigma_{3R}$$

Here, R stands for reference, S stands for samples, σ_{3s} is the three-photon absorption cross section, Q is quantum yield, c is the concentration, n is refractive index, and F is three-photon fluorescence integral area. The absolute value of the three-photon absorption cross section of Rhodamin 6G is $4.3\pm3\times10^{-81}$ $cm^6s^2photon^{-2}$.[2]

1.8 Multi-photon absorption open aperture Z-scan measurements.

The laser pulses were produced by Laser: Coherent Astrella+TOPAS Prime (1600-2700nm, 1kHz, 120fs, which focused onto a 1-mm-thick quartz cuvette containing the solutions of the derivatives. The incident and transmitted laser pulse energy were monitored by moving the cuvette along the propagation direction of the laser pulses. Z-scans displayed a symmetric valley with respect to the focus, typical of an induced positive NLA effect. By fitting the trances of Z-scan theories by three-photon theory, we obtained the nonlinear absorption coefficient *γ* (3PA) at different levels of I_0.[3,4]

Theory:

$$\gamma = \frac{I_0^2 / I^2 - 1}{2 \times L \times I_0^2}$$

$$\delta_{3s} = \frac{\gamma}{N_A \times d_0 \times 10^{-3}} \times \left(\frac{hc}{\lambda}\right)_{n-1}$$

Here, δ_{3s} is the three-photon absorption cross section, γ is three photon absorption coefficients, λ is wavelength of incident light, N_A is the Avogadro constant, d_0 is the concentration of the sample, and n is the number of absorbed photons (*n* = 2/3).

1.9 Characterizations.

All UV-vis optical absorption spectra of nanoclusters dissolved in CH_2Cl_2 were recorded using an Agilent 8453 diode array spectrometer, whose background correction was made using a CH_2Cl_2 blank. Nanocluster samples were dissolved in CH_2Cl_2 to make dilute solutions, followed by

spectral measurement (1 cm path length quartz cuvette).

Photoluminescence (PL) spectra were measured on an FL-4500 spectrofluorometer with the same optical density (OD) of ~0.1.

Quantum yields (QYs) were measured with dilute solutions of nanoclusters on a HORIBA FluoroMax-4P.

X-ray photoelectron spectroscopy (XPS) measurements were performed on a Thermo ESCALAB 250 configured with a monochromatized Al Kα (1486.8 eV) 150 W X-ray source, 0.5 mm circular spot size, flood gun to counter charging effects, and analysis chamber base pressure lower than 1×10^{-9} mbar.

1.10 Computational details.

The ground state structure of the clusters were calculated using DFT with B3LYP functional and Lan2dz basis set. The initial geometries of the clusters were generated by the Gauss View software. All of these calculations were performed with Gaussian 09.

1.11 Data availability.

The X-ray crystallographic coordinates for structure reported in this work has been deposited at the Cambridge Crystallographic Data Center (CCDC), under deposition number CCDC-2223274. These data can be obtained free of charge from the Cambridge Crystallographic Data Centre via www.ccdc.cam.ac.uk/data_request/cif, which has been mentioned in the article.

References:

[1] M. Pawlicki, H. A. Collins, R. G. Denning, H. L. Anderson. Two-Photon Absorption and the Design of Two-Photon Dyes. *Angew. Chem. Int. Ed.* **2009**, *48*, 3244-3266.

[2] Z. Feng, D. Li, M. Zhang, T. Shao, Y. Shen, X. Tian, Q. Zhang, S. Li, J. Wu, Y. Tian. Enhanced Three-Photon Activity Triggered by the AIE Behavior of a Novel Terpyridine-Based Zn(II) Complex Bearing a Thiophene Bridge. *Chem. Sci.* **2019**, *10*, 7228-7232.

[3] D. S. Corre, L. De Boni, L. Misoguti, I. Cohanoschi, F. E. Hernandez, C. R. Mendonc. Z-scan Theoretical Analysis for Three-, Four- and Five-Photon Absorption. *Opt. Express* **2007**, *277*, 440-445.

[4] G. C. Xing, W. Ji, Y. Zheng, J. Y. Ying. High Efficiency and Nearly Cubic Power Dependence of Below-Band-Edge Photoluminescence in Water-Soluble, Copper doped ZnSe/ZnS Quantum Dots. *Opt. Express* **2008**, *16*, 5715-5720.

2. Figures and tables

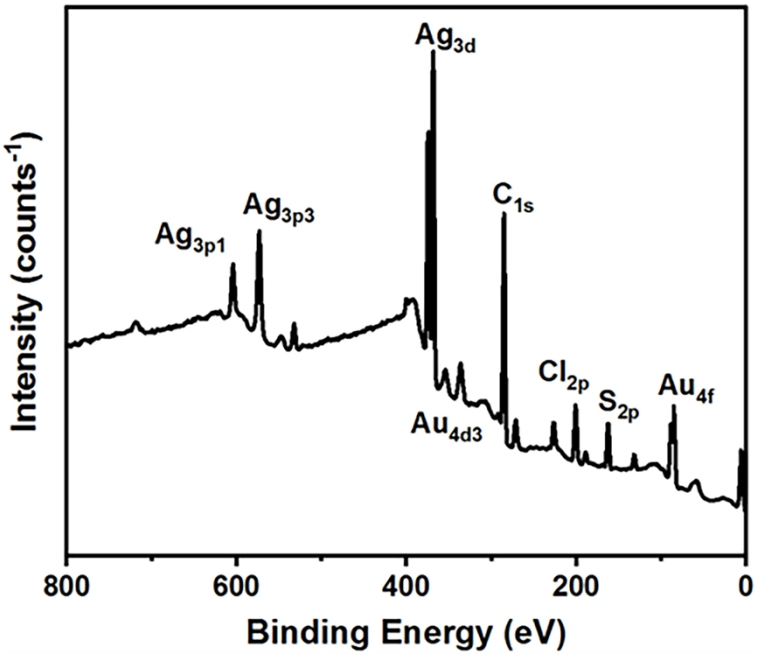

Fig. S1 XPS result of the $Au_4Ag_{13}(DPPM)_3(SPhCl_2)_9$ nanocluster. The experimental Au:Ag ratio was determined as 24.3%:75.7%, matching well with the theoretical value (23.5%:76.5%).

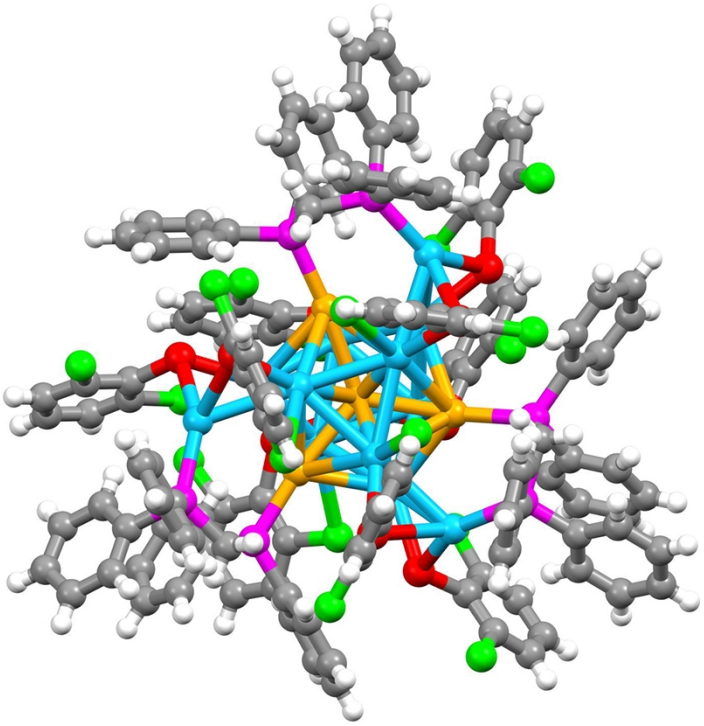

Fig. S2 Total structure of the $Au_4Ag_{13}(DPPM)_3(SPhCl_2)_9$ nanocluster. No counterion was observed in the crystal lattice of the nanocluster, suggesting the electroneutrality of this nanocluster. Color labels: yellow = Au; blue = Ag; red = S; magenta = P; green = Cl; grey = C; white = H.

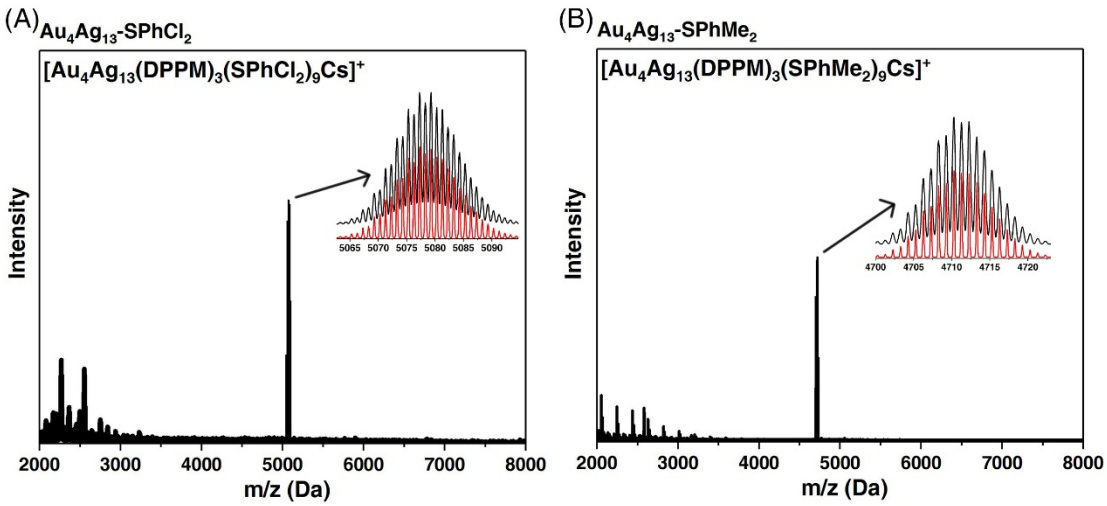

Fig. S3 ESI-MS results of (A) $Au_4Ag_{13}(DPPM)_3(SPhCl_2)_9$ and (B) $Au_4Ag_{13}(DPPM)_3(SPhMe_2)_9$ nanoclusters. Insets: experimental (in black) and simulated (in red) isotope patterns.

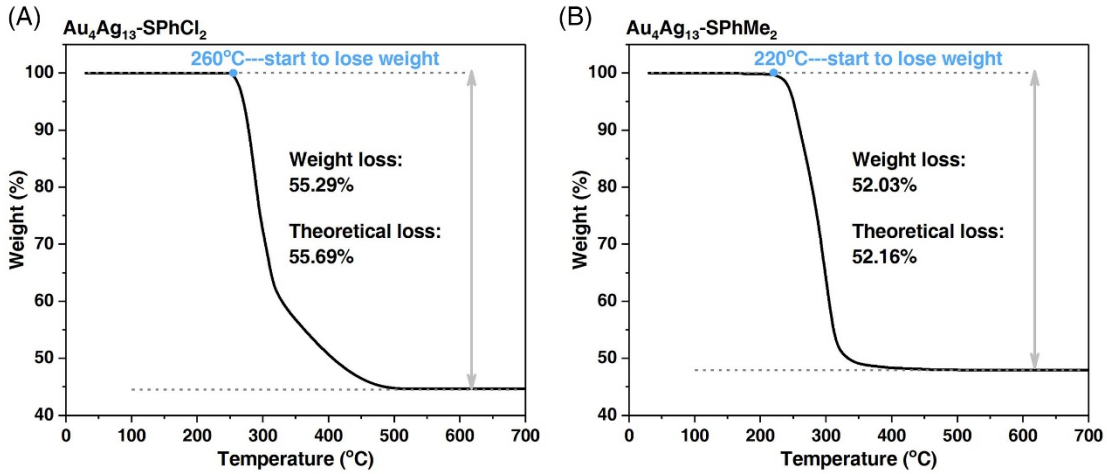

Fig. S4 TGA results of (A) $Au_4Ag_{13}(DPPM)_3(SPhCl_2)_9$ and (B) $Au_4Ag_{13}(DPPM)_3(SPhMe_2)_9$ nanoclusters. The TGA results suggested that the $Au_4Ag_{13}(DPPM)_3(SPhMe_2)_9$ started to lose weight at 220°C, much lower than that of $Au_4Ag_{13}(DPPM)_3(SPhCl_2)_9$ (260°C), demonstrating the enhanced thermal stability of the $Au_4Ag_{13}(DPPM)_3(SPhCl_2)_9$ nanocluster.

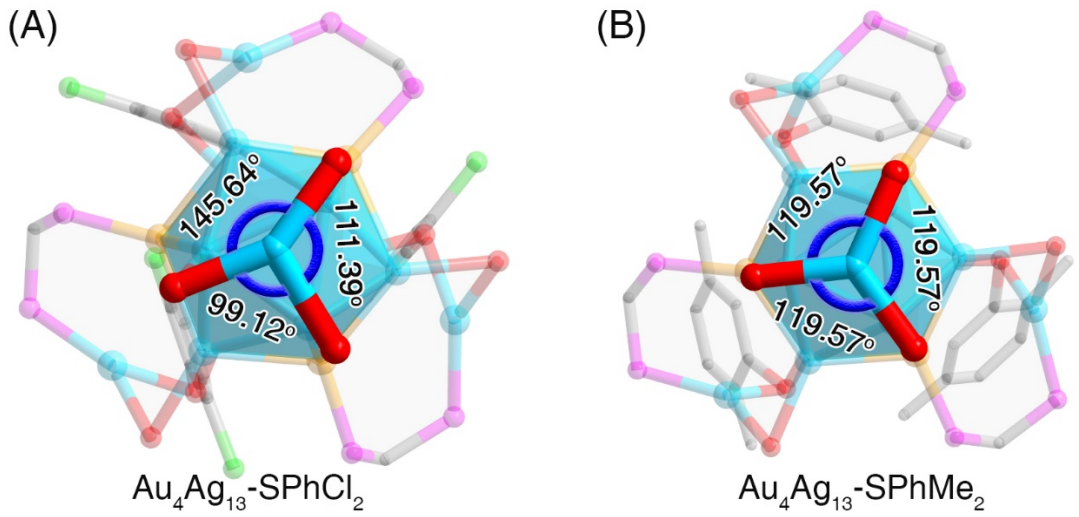

Fig. S5 Comparison of the corresponding rotation angles in (A) $Au_4Ag_{13}(DPPM)_3(SPhCl_2)_9$ and (B) $Au_4Ag_{13}(DPPM)_3(SPhMe_2)_9$ nanoclusters. The rotation angles were 145.64°, 111.39°, and 99.12° for the $Au_4Ag_{13}(DPPM)_3(SPhCl_2)_9$ nanocluster. By comparison, the corresponding rotation angles were the same as 119.57° for the $Au_4Ag_{13}(DPPM)_3(SPhMe_2)_9$ nanocluster. Color labels: yellow = Au; blue = Ag; red = S; magenta = P; green = Cl; grey = C.

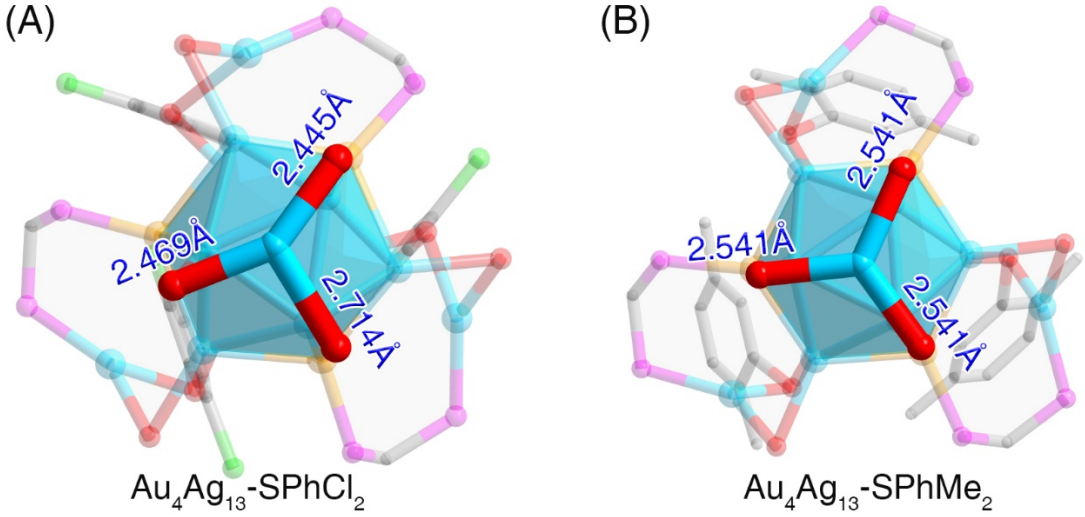

Fig. S6 Comparison of the corresponding Ag-S bong lengths in (A) $Au_4Ag_{13}(DPPM)_3(SPhCl_2)_9$ and (B) $Au_4Ag_{13}(DPPM)_3(SPhMe_2)_9$ nanoclusters. The Ag-S bond lengths in the $Ag_1(SPhCl_2)_3$ unit followed an uneven distribution in the $Au_4Ag_{13}(DPPM)_3(SPhCl_2)_9$ nanocluster (2.469 Å, 2.445 Å, and 2.714 Å) while an even distribution in the $Au_4Ag_{13}(DPPM)_3(SPhMe_2)_9$ nanocluster (2.541 Å, 2.541 Å, and 2.541 Å,). Color labels: yellow = Au; blue = Ag; red = S; magenta = P; green = Cl; grey = C.

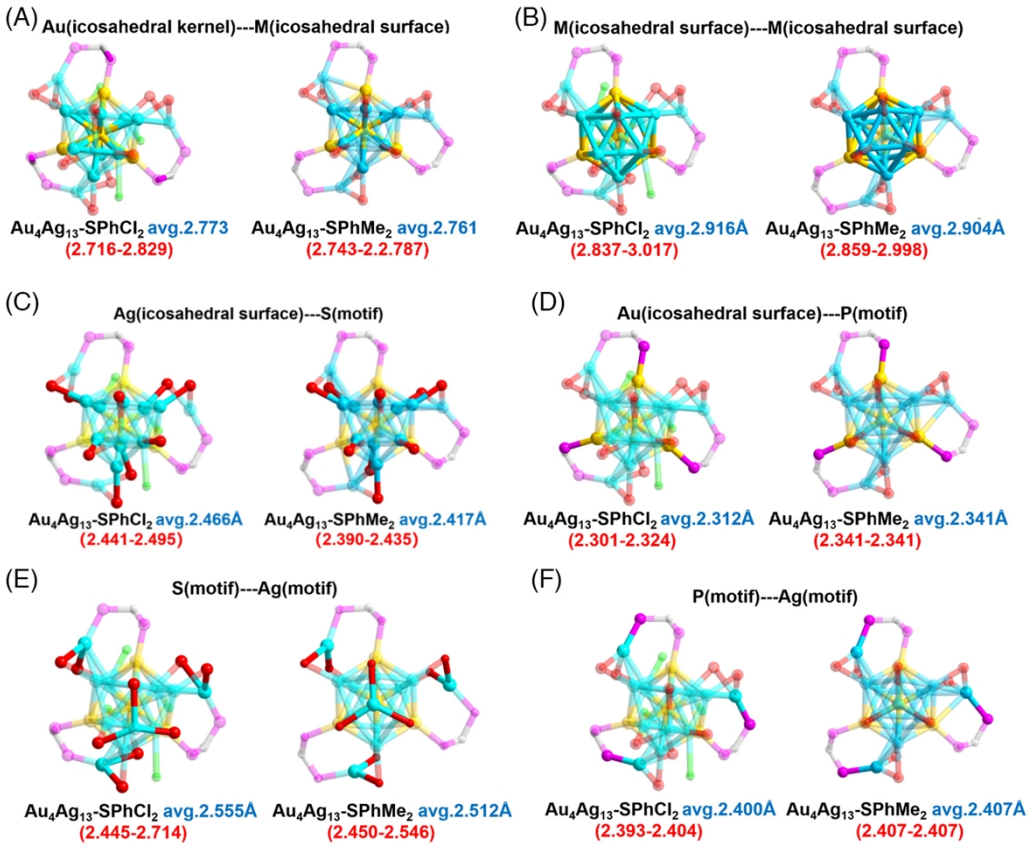

Fig. S7 Comparison of the corresponding bond lengths between $Au_4Ag_{13}(DPPM)_3(SPhCl_2)_9$ and $Au_4Ag_{13}(DPPM)_3(SPhMe_2)_9$ nanoclusters. (A) Comparison of the length of Au(icosahedral kernel)---Au/Ag(icosahedral surface) bonds. (B) Comparison of the length of Au/Ag(icosahedral surface)---Au/Ag(icosahedral surface) bonds. (C) Comparison of the length of Ag(icosahedral surface)---S(motif) bonds. (D) Comparison of the length of Au(icosahedral surface)---P(motif) bonds. (E) Comparison of the length of S(motif)---Ag(motif) bonds. (F) Comparison of the length of P(motif)---Ag(motif) bonds.

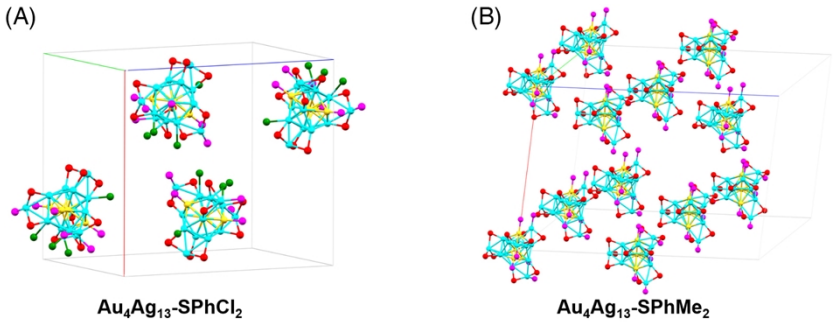

(C)

	Au_4Ag_{13}-$SPhCl_2$	Au_4Ag_{13}-$SPhMe_2$
Crystal System	monoclinic	hexagonal
Space Group	*P 21/n*	*R 3c*
a,b,c/Å	24.1353(4), 24.3999(4) , 26.5043(4)	27.7997(17) , 27.7997(17) , 41.611(3)
α, β, γ/°	90, 90.951(1), 90	90, 90, 120
Volume/Å^3	15606.2(4)	27849.6(3)
Density(gcm^{-1})	2.105	1.635
Z	4	6

Fig. S8 Crystal lattices of (A) $Au_4Ag_{13}(DPPM)_3(SPhCl_2)_9$ and (B) $Au_4Ag_{13}(DPPM)_3(SPhMe_2)_9$ nanoclusters. (C) Comparison of the crystalline unit cell parameters between $Au_4Ag_{13}(DPPM)_3(SPhCl_2)_9$ and $Au_4Ag_{13}(DPPM)_3(SPhMe_2)_9$ nanoclusters.

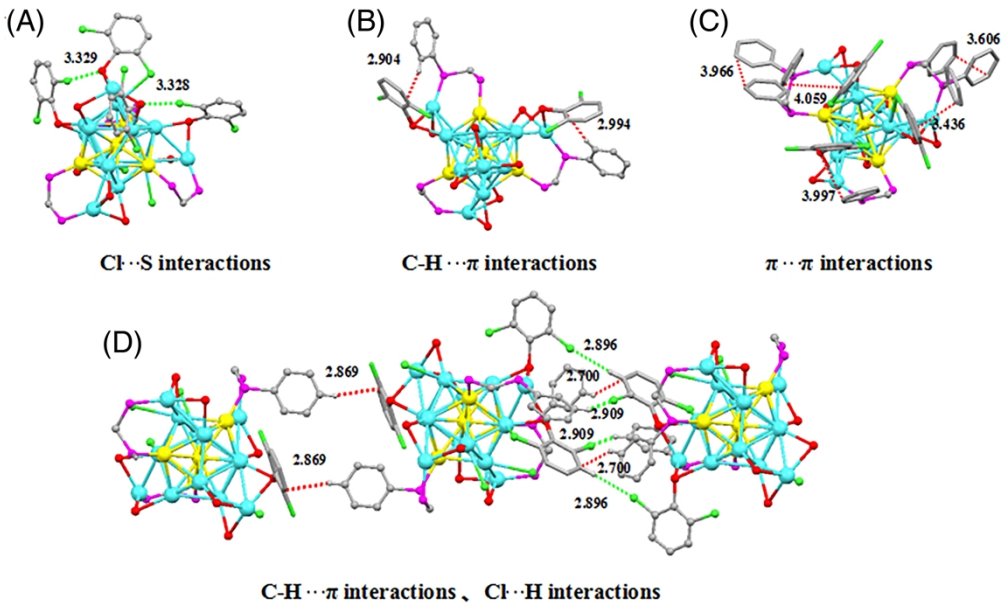

Fig. S9 Intramolecular and intermolecular interactions of $Au_4Ag_{13}(DPPM)_3(SPhCl_2)_9$. (A) Intramolecular Cl···S interactions. (B) Intramolecular C-H···π interactions. (C) Intramolecular π···π interactions. (D) Intermolular C-H···π and Cl···H interactions.

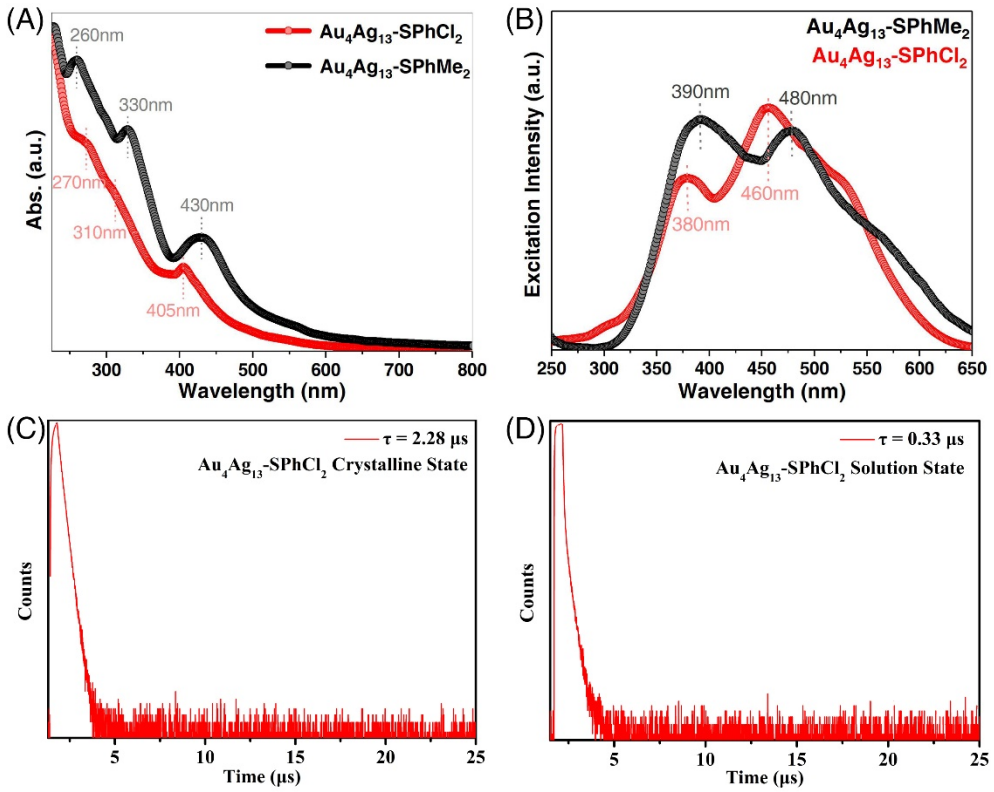

Fig. S10 (A) Comparison of the optical absorptions between $Au_4Ag_{13}(DPPM)_3(SPhCl_2)_9$ and $Au_4Ag_{13}(DPPM)_3(SPhMe_2)_9$ nanoclusters (dissolved in CH_2Cl_2). (B) Excitation spectra of $Au_4Ag_{13}(DPPM)_3(SPhCl_2)_9$ and $Au_4Ag_{13}(DPPM)_3(SPhMe_2)_9$ nanoclusters. (C) Fluorescence lifetime of $Au_4Ag_{13}(DPPM)_3(SPhCl_2)_9$ in its crystalline state. (D) Fluorescence lifetime of $Au_4Ag_{13}(DPPM)_3(SPhCl_2)_9$ in its solution state.

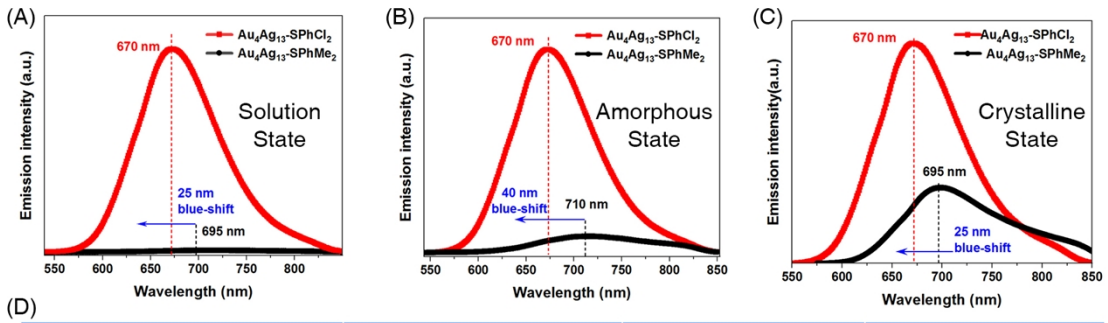

(D)

	Solution State (CH_2Cl_2)	Amorphous State	Crystalline State
$Au_4Ag_{13}(DPPM)_3(SPhMe_2)_9$	QY=0.0041%	QY=1.14%	QY=2.68%
$Au_4Ag_{13}(DPPM)_3(SPhCl_2)_9$	QY=11.78%	QY=32.29%	QY=52.60%

Fig. S11 Comparison of the photoluminescence between $Au_4Ag_{13}(DPPM)_3(SPhCl_2)_9$ and $Au_4Ag_{13}(DPPM)_3(SPhMe_2)_9$ nanoclusters in (A) solution, (B) amorphous, and (C) crystalline states. (D) Comparison of the photoluminescence quantum yields between $Au_4Ag_{13}(DPPM)_3(SPhCl_2)_9$ and $Au_4Ag_{13}(DPPM)_3(SPhMe_2)_9$ nanoclusters in different states.

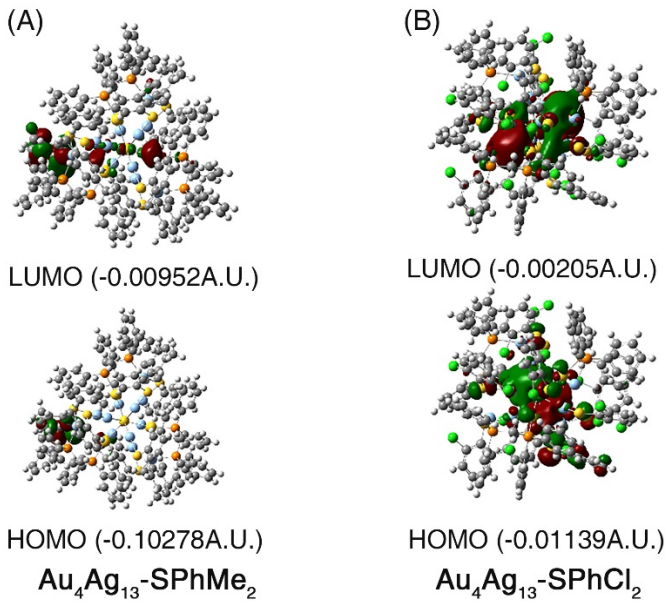

Fig. S12 Molecular orbital energy diagrams of (A) Au_4Ag_{13}-$SPhMe_2$ and (B) Au_4Ag_{13}-$SPhCl_2$ nanoclusters.

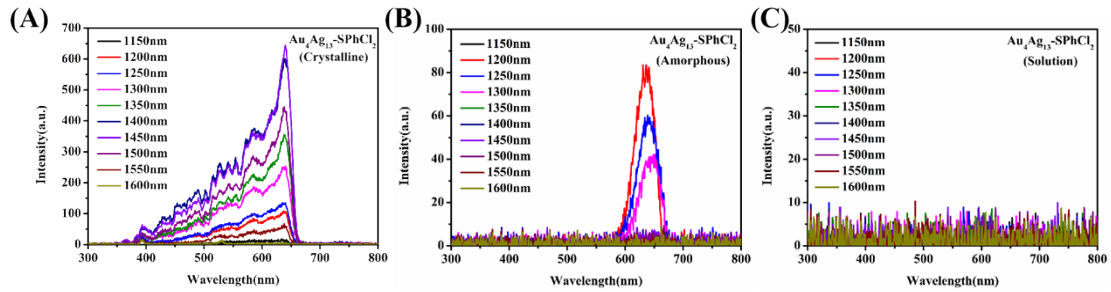

Fig. S13 (A) Fluorescence intensity of Au_4Ag_{13}-$SPhCl_2$ in the crystalline state (3PEF). Excitation: 1150-1600 nm. (B) Fluorescence intensity of Au_4Ag_{13}-$SPhCl_2$ in the amorphous state (2PEF). Amorphous: 10mM. Excitation: 1150-1600 nm. (C) Fluorescence intensity of Au_4Ag_{13}-$SPhCl_2$ in the solution state. Solution: 1mM. Excitation: 1150-1600 nm.

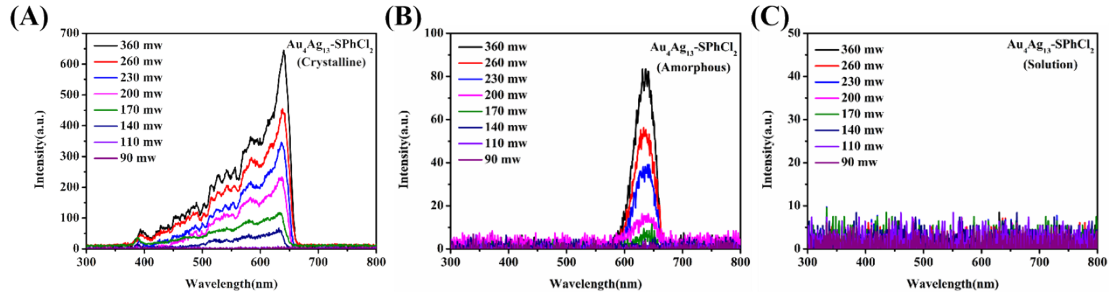

Fig. S14 (A) Fluorescence intensity of Au_4Ag_{13}-$SPhCl_2$ at different powers in the crystalline state (360 mW-90 mW, 1450 nm). (B) Fluorescence intensity of Au_4Ag_{13}-$SPhCl_2$ at different powers in the amorphous state (360 mW-90 mW, 1200 nm). Amorphous: 10mM. (C) Fluorescence intensity of Au_4Ag_{13}-$SPhCl_2$ at different powers in the solution state (360 mW-90 mW). Solution: 1mM.

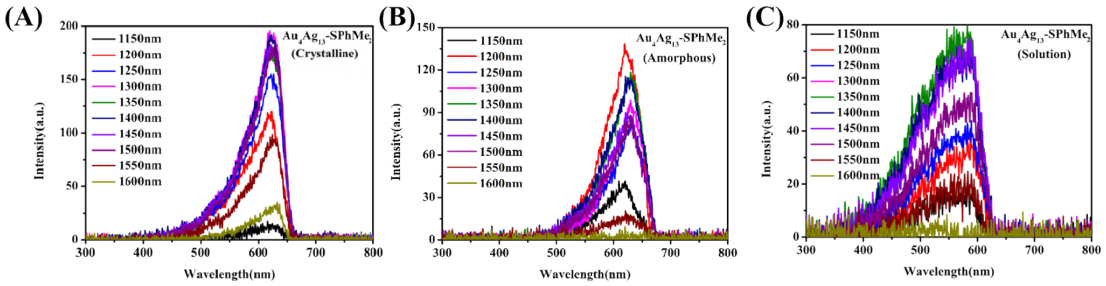

Fig. S15 (A) Fluorescence intensity of Au_4Ag_{13}-$SPhMe_2$ in the crystalline state (3PEF). Excitation: 1150-1600 nm. (B) Fluorescence intensity of Au_4Ag_{13}-$SPhMe_2$ in the amorphous state (2PEF). Amorphous: 10mM. Excitation: 1150-1600 nm. (C) Fluorescence intensity of Au_4Ag_{13}-$SPhMe_2$ in the solution state (2PEF). Solution: 1mM. Excitation: 1150-1600 nm.

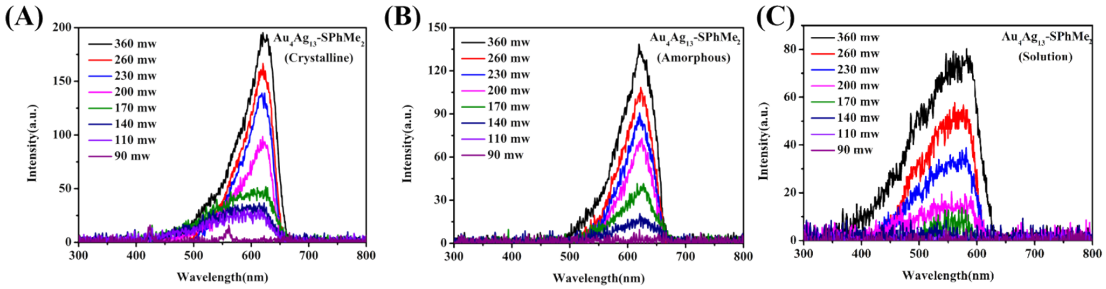

Fig. S16 (A) Fluorescence intensity of Au_4Ag_{13}-$SPhMe_2$ at different powers in the crystalline state (360mW - 90mW, 1300 nm). (B) Fluorescence intensity of Au_4Ag_{13}-$SPhMe_2$ at different powers in the amorphous state (360mW - 90mW, 1200 nm). Amorphous: 10mM. (C) Fluorescence intensity of Au_4Ag_{13}-$SPhMe_2$ at different powers in the solution state (360mW - 90mW, 1350 nm). Solution: 1mM.

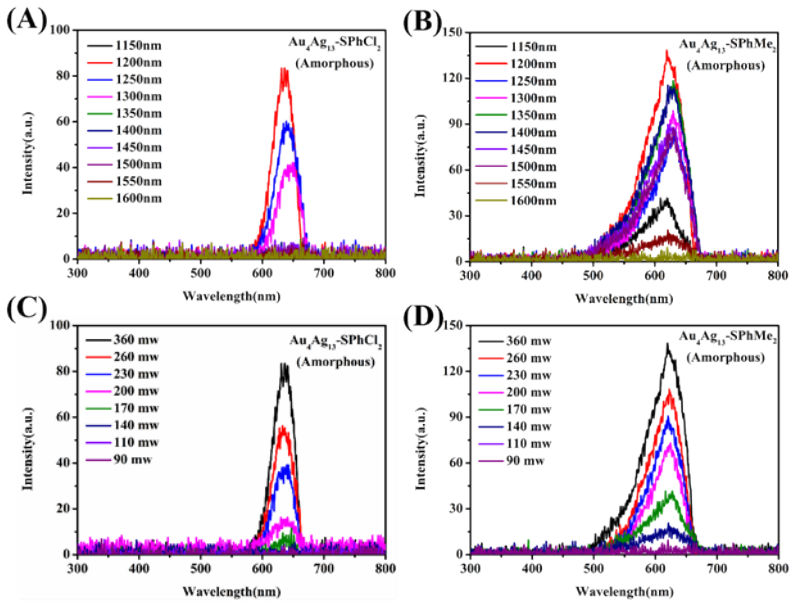

Fig. S17 (A) Fluorescence intensity of Au_4Ag_{13}-$SPhCl_2$ in the amorphous state (2PEF). Amorphous: 10mM. Excitation: 1150-1600 nm. (B) Fluorescence intensity of Au_4Ag_{13}-$SPhMe_2$ in the amorphous state (2PEF). Amorphous: 10mM. Excitation: 1150-1600 nm. (C) Fluorescence intensity of Au_4Ag_{13}-$SPhCl_2$ at different powers in the amorphous state (360mW - 90mW, 1200 nm). Amorphous: 10mM. (D) Fluorescence intensity of Au_4Ag_{13}-$SPhMe_2$ at different powers in the amorphous state (360mW - 90mW, 1200 nm). Amorphous: 10mM.

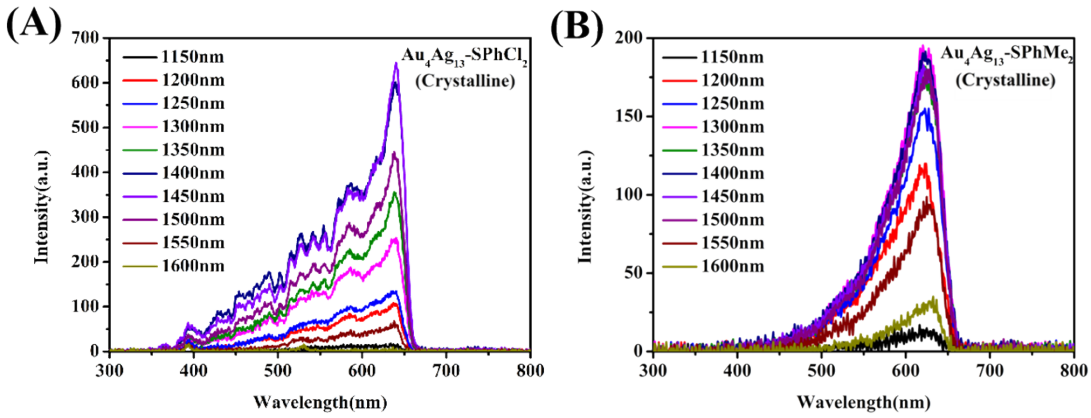

Fig. S18 (A) Fluorescence intensity of Au_4Ag_{13}-$SPhCl_2$ in the crystalline state (3PEF). Excitation: 1150-1600 nm. (B) Fluorescence intensity of Au_4Ag_{13}-$SPhMe_2$ in the crystalline state (3PEF). Excitation: 1150-1600 nm.

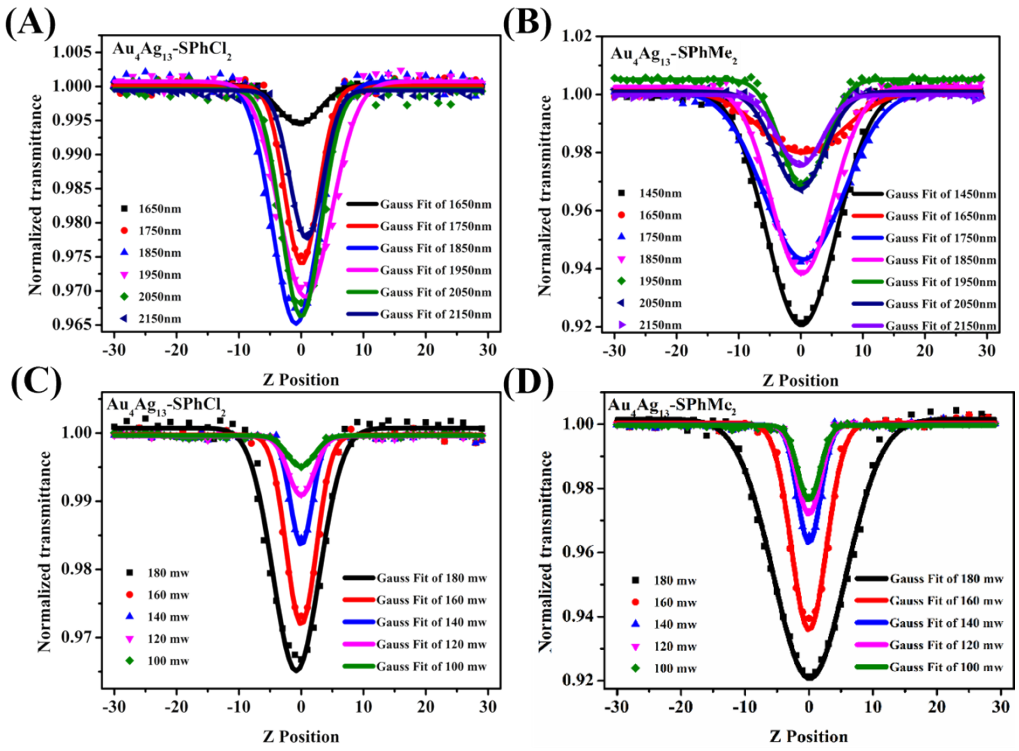

Fig. S19 (A) Three-photon Z-scan of Au_4Ag_{13}-$SPhCl_2$ in the solution state. Solution: 1mM. (B) Three-photon Z-scan of Au_4Ag_{13}-$SPhMe_2$ in the solution state. Solution: 1mM. (C) Z-scan of Au_4Ag_{13}-$SPhCl_2$ at different powers in the solution state (180mW - 100mW, 1850 nm). Solution: 1mM. (D) Z-scan of Au_4Ag_{13}-$SPhMe_2$ at different powers in the solution state (180mW - 100mW, 1450 nm). Solution: 1mM.

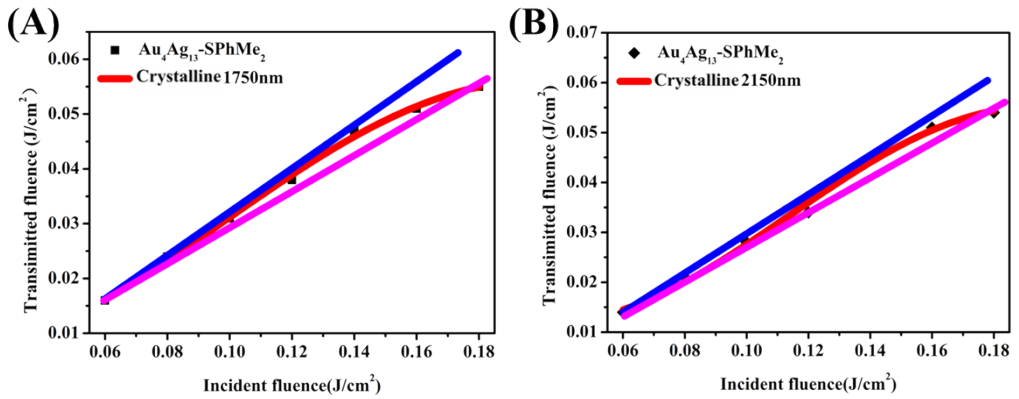

Fig. S20 (A) Optical limit response of Au_4Ag_{13}-$SPhMe_2$ in the crystalline state (1750 nm). The black squares represent experimental data and the red curves represent theoretical data. (B) Optical limit response of Au_4Ag_{13}-$SPhMe_2$ in the crystalline state (2150 nm). The black squares represent experimental data and the red curves represent theoretical data.

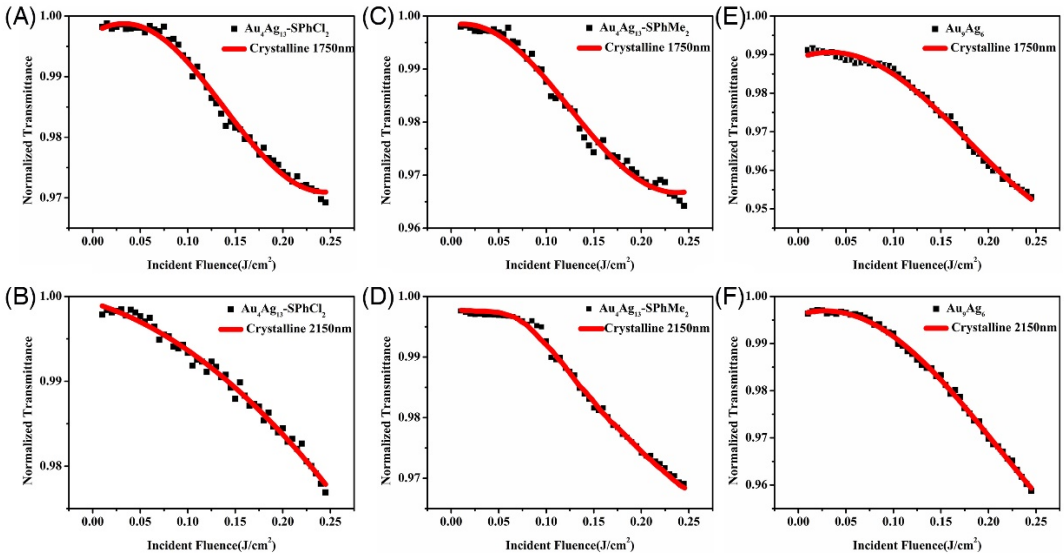

Figure S21. (A) Optical limit response (RSA) of Au_4Ag_{13}-$SPhCl_2$ crystals (1750 nm). (B) RSA of Au_4Ag_{13}-$SPhCl_2$ crystals (2150 nm). (C) RSA of Au_4Ag_{13}-$SPhMe_2$ crystals (1750 nm). (D) RSA of Au_4Ag_{13}-$SPhMe_2$ crystals (2150 nm). (E) RSA of Au_9Ag_6 crystals (1750 nm). (F) RSA of Au_9Ag_6 crystals (2150 nm). The black squares represent experimental data and the red curves represent theoretical data.

Table S1. Crystal data and structure refinement for the $Au_4Ag_{13}(DPPM)_3(SPhCl_2)_9$ nanocluster. The CCDC number of the $Au_4Ag_{13}(DPPM)_3(SPhCl_2)_9$ nanocluster is 2223274.

Molecular formula	$C_{129}H_{93}Ag_{13}Au_4Cl_{18}P_6S_9$
Crystal system	monoclinic
Space group	P 21-n
a/Å	24.1353(4)
b/Å	24.3999(4)
c/Å	26.5043(4)
α/°	90
β/°	90.951(1)
γ/°	90
Volume/Å^3	15606.2(4)
Z	4
ρ_{calc}g/cm^3	2.105
μ/mm^{-1}	24.508
F(000)	9336
Radiation	CuK\a (λ = 1.54186)
Index ranges	-20 ≤ h ≤27, -25 ≤ k ≤28, -22 ≤ l ≤ 30
θ range (°)	3.34 –70.16
Measured reflections and unique reflections	24713 / 17662 (*Rint = 0.0564, Rsigma =0.0719*)
Goodness-of-fiton F^2	0.924
Largest diff. peak/hole / e Å^{-3}	2.698 / -1.928
Final R indexes [I>=2σ (I)]	R_1 = 0.0443, wR_2 = 0.1028
Final R indexes [all data]	R_1 = 0.0632, wR_2 = 0.1078

Table S2. Comparison of NLA coefficient γ.

1750 nm	I_0 (W/cm^2)	γ (×10^{-21}cm^3/W^2)
Au_4Ag_{13}-$SPhCl_2$	0.2632	78.3427
Au_4Ag_{13}-$SPhMe_2$	0.2505	93.3251
Au_9Ag_6	-	-
2150 nm	I_0 (W/cm^2)	γ (×10^{-21}cm^3/W^2)
Au_4Ag_{13}-$SPhCl_2$	0.2662	87.8899
Au_4Ag_{13}-$SPhMe_2$	0.2505	94.7191
Au_9Ag_6	0.2632	101.1236

Table S3. Comparison of the linear and nonlinear scattering coefficients of Au_4Ag_{13}-$SPhCl_2$ and Au_4Ag_{13}-$SPhMe_2$ nanoclusters.

Au_4Ag_{13} -$SPhCl_2$	I_0 (W/cm^2)	γ ($\times10^{-21}$cm^3/W^2)	**Au_4Ag_{13} -$SPhMe_2$**	I_0 (W/cm^2)	γ ($\times10^{-21}$cm^3/W^2)
1650 nm	0.1891	15.4426	1450 nm	0.4347	111.8846
1750 nm	0.2632	78.3427	1650 nm	0.1891	56.4428
1850 nm	0.3913	79.5985	1750 nm	0.2505	93.3251
1950 nm	0.3043	68.5983	1850 nm	0.3913	78.9126
2050 nm	0.3478	72.9431	1950 nm	0.3043	73.8428
2150nm	0.2662	55.6925	2050 nm	0.3478	77.3013
			2150nm	0.2505	94.7191
Au_4Ag_{13} -$SPhCl_2$ (1850nm)	I_0 (W/cm^2)	γ ($\times10^{-21}$cm^3/W^2)	**Au_4Ag_{13} -$SPhMe_2$ (1450nm)**	I_0 (W/cm^2)	γ ($\times10^{-21}$cm^3/W^2)
0.18 W	0.3913	79.5985	0.18 W	0.3913	82.5917
0.16 W	0.3478	52.5814	0.16 W	0.3478	74.6348
0.14 W	0.3043	33.7863	0.14 W	0.3043	48.6458
0.12 W	0.2609	23.5469	0.12 W	0.2609	43.2359
0.10 W	0.2174	14.4358	0.10 W	0.2174	42.2639
Au_4Ag_{13} -$SPhCl_2$	α (cm^{-1})		**Au_4Ag_{13} -$SPhMe_2$**	α (cm^{-1})	
	0.3733			0.1643	

Table S4. Comparison of optical limiting onset values.

1750 nm	OL (J/cm^2)		**2150 nm**	OL (J/cm^2)
Au_4Ag_{13}-$SPhCl_2$	0.0705		Au_4Ag_{13}-$SPhCl_2$	0.0627
Au_4Ag_{13}-$SPhMe_2$	0.0563		Au_4Ag_{13}-$SPhMe_2$	0.0749
Au_9Ag_6	0.0352		Au_9Ag_6	0.0445